A&A, 710, A120 (2026)
https://doi.org/10.1051/0004-6361/202558812

Astronomy & Astrophysics

Phase spirals induced by the gas warp

Shuyu Wang (汪书玉)[1,⋆], Anthony G. A. Brown[1], Victor P. Debattista[2], and Tigran Khachaturyants[3]

[1] Leiden Observatory, Leiden University, Einsteinweg 55, 2333 CC Leiden, The Netherlands
[2] Jeremiah Horrocks Institute, University of Lancashire, Preston PR1 2HE, UK
[3] Department of Astronomy, Shanghai Jiao Tong University, 800 Dongchuan Road, Shanghai 200240, PR China

Received 29 December 2025 / Accepted 5 April 2026

ABSTRACT

Context. The discovery of the phase space-spirals in the Solar neighborhood in *Gaia* Data Release 2 has prompted various attempts to understand their origin. A source of bending waves that has been neglected as a cause of the phase spiral is irregular gas inflow along the warp.

Aims. We studied whether perturbations by the gas warp could induce phase spirals. Accounting for this additional formation scenario for phase spirals could improve our current understanding of the perturbation history of the Milky Way disk.

Methods. We used two *N*-body–smoothed particle hydrodynamics (SPH) simulations of an isolated galaxy to search for and study warp-induced phase spirals. We studied the emergence and propagation of the detected phase spirals using Fourier decomposition.

Results. We detect strong one-armed phase spirals in the warped simulation. These phase spirals are prevalent and persist over ~10 Gyr. The morphology of these phase spirals varies with location and evolves with time. In particular, the emergence rate of the phase spiral evolves with the gas inflow at the outer disk and the bending wave amplitude, indicating that these phase spirals are a record of warp-induced bending waves. We find that these phase spirals can reach amplitudes comparable to those in the *Gaia* DR3. We only detect weak and stochastically distributed phase spirals in an unwarped control simulation.

Conclusions. We conclude that phase spirals can be induced by irregular gas accretion along the warp. These phase spirals occur globally and are long-lived.

Key words. stars: kinematics and dynamics – galaxy: disk – galaxy: kinematics and dynamics

1. Introduction

Antoja et al. (2018) discovered the "phase spiral" – a coherent spiral pattern in the vertical phase space of the Solar neighborhood – using *Gaia* DR2 data (Gaia Collaboration 2018). This one-armed phase spiral was observed in the Z–V_z phase space map weighted by stellar number density, median radial velocity, or median azimuthal velocity. The discovery provides compelling evidence for the dynamically perturbed state of the Milky Way disk and ongoing phase mixing in the Solar neighborhood.

Subsequent observational work endeavored to map the phase spirals across the Galactic disk. The increased sample size and improved astrometric precision provided by the *Gaia* DR3 (Gaia Collaboration 2023b) allowed the identification of a sharper signature in an extended sample (Antoja et al. 2023) and the mapping of phase spirals across the Galactic radius and azimuth. Hunt et al. (2022) split a *Gaia* DR3 sample within a cylindrical distance $d_{\rm cyl} \leq 1$ kpc from the Sun into dynamically local groups in azimuthal action (guiding center radius) and angle space. This division spans a wide range of guiding center radii and reveals a two-armed phase spiral signature in the inner Galactic disk.

Various formation scenarios have been proposed for the one-armed (two-armed) phase spirals, which are typically associated with the vertical bending (breathing) waves in the Galaxy. The most prevalent hypothesis is that one-armed phase spirals arise from the recent passage of the Sagittarius dwarf galaxy (Sgr) (e.g., Binney & Schönrich 2018; Bland-Hawthorn et al. 2019; Laporte et al. 2019; Bland-Hawthorn & Tepper-García 2021; Hunt et al. 2021; Asano et al. 2025). One-armed phase spirals may also result from the dark matter wake produced by the Large Magellanic Cloud (LMC) (Grand et al. 2023). They may also be induced by internal processes, such as buckling of the Galactic bar (Khoperskov et al. 2019). Additionally, one-armed phase spirals may arise from the combined effect of stochastic heating by dark matter (DM) subhalos (Tremaine et al. 2023; Gilman et al. 2025; Tepper-García et al. 2025). A slowing bar (Li et al. 2023) or transient spiral arms (Hunt et al. 2022; Banik et al. 2023) may be responsible for the presence of two-armed phase spirals. Chiba et al. (2025) proposed that two-armed phase spirals could naturally form by the combined effects of vertical resonances and stochastic kicks. The two-armed phase spirals may also be excited by the tidally-induced spiral arms (Asano et al. 2025). Lin et al. (2025) suggested that the observed two-armed phase spiral signatures could be a superposition of one-armed phase spiral signatures from multiple previous perturbations. Hunt & Vasiliev (2025) provide a comprehensive review of the proposed formation scenarios for phase spirals.

Characteristics of phase spirals, such as their degree of winding, amplitude, and dominant Fourier modes, provide clues to the past perturbation events in the Milky Way disk (e.g., Darragh-Ford et al. 2023; Widmark et al. 2025) and the Galactic potential (e.g., Widmark et al. 2021; Guo et al. 2024). For example, in the single-impact origin scenario, the degree of winding of the phase spirals could reveal the impact time – the time elapsed since the impact seeded the vertical corrugations. By "rewinding" the phase spirals, Antoja et al. (2023) and Frankel et al. (2023) estimate a Sagittarius impact time of a few hundred Myr ago. However, these estimates do not include the effect of

⋆ Corresponding author: shuyuwang.astro@gmail.com

self-gravity, which can significantly reduce the winding rate of phase spirals (Darling & Widrow 2018; Widrow 2023). Self-consistent models further demonstrate that phase spirals commonly emerge with a delay time of a few hundred Myr after the most recent impact (e.g., Bland-Hawthorn & Tepper-García 2021; Hunt et al. 2021; Asano et al. 2025), implying that earlier works may have systematically underestimated the impact time.

While the above studies demonstrate the plausibility of various formation scenarios for phase spirals, none quantitatively reproduces the *Gaia* phase spirals. For instance, the hypothesis that the Sgr passage alone could produce the *Gaia* phase spirals would require a massive Sgr progenitor (on the order of $10^{10} M_\odot$; Bland-Hawthorn et al. 2019; Laporte et al. 2019), which cannot be reconciled with the observed low mass of the current-day Sgr remnant ($\sim 4 \times 10^8$ $M_\odot$; Vasiliev & Belokurov 2020). Similarly, Gilman et al. (2025) suggest that while stochastic heating by multiple dark matter subhalos (Tremaine et al. 2023) could result in a significant perturbation, it fails to reach the amplitude of the *Gaia* phase spirals.

Another source of perturbation is misaligned gas accretion. García-Conde et al. (2022) and García-Conde et al. (2024) identify phase spirals in a cosmological environment with infalling satellite galaxies, a misaligned dark matter halo, minor dark matter subhalos, and misaligned gas accretion. Khachaturyants et al. (2022a) discovered that misaligned gas accretion induces long-lived bending waves in an isolated warped galaxy simulation. These vertical corrugations may manifest as spiral patterns in phase space, although the question of whether the warp can excite phase spirals was not explored.

In this work, we present the discovery of phase spirals in the isolated warped galaxy simulation of Khachaturyants et al. (2022a). We propose that misaligned gas accretion along the Galactic warp is a viable mechanism for forming phase spirals. Although we do not attempt to quantitatively reproduce the *Gaia* observations, we detect warp-induced phase spirals that are qualitatively similar to the observed phase spirals. This new formation channel might also contribute to the "everything" option, where the combined effect of multiple perturbers gives rise to the observed phase spirals (see, e.g., Hunt & Vasiliev 2025; Widmark et al. 2025). The proposed mechanism could deepen our understanding of the perturbation history of the Galactic disk.

This work focuses on the stellar disk, which is the main component in which the phase-space structure has been studied observationally. This paper is organized as follows. In Sect. 2, we briefly recapitulate the simulations. In Sect. 3, we describe the method for identifying phase spirals in the simulations, which is adapted from García-Conde et al. (2022) and Tepper-García et al. (2025). In Sect. 4, we present the detected phase spirals in the warped galaxy, their spatial variation, and their time evolution. In Sect. 5, we discuss several characteristics of the detected phase spirals and provide a qualitative comparison between our results and the *Gaia* observations. We summarize our results in Sect. 6.

2. Simulations

We used two *N*-body–smoothed particle hydrodynamics (SPH) simulations presented in Khachaturyants et al. (2022a). We evolved both models using the SPH code GASOLINE (Wadsley et al. 2004); one model developed a warp through an initially misaligned gaseous corona, while the other remained unwarped throughout its evolution.

The warped simulation of Khachaturyants et al. (2022a) follows the method of Debattista et al. (2015), where the merger of two identical spherical Navarro-Frenk-White (Navarro et al. 1996) dark matter halos creates a triaxial dark matter halo whose embedded gaseous corona has an angular momentum misaligned with respect to the halo's principal axes.

Each progenitor halo has a virial mass and radius of $M_{200} = 8.7 \times 10^{11}$ $M_\odot$ and $r_{200} = 196$ kpc at $z = 0$, with a co-spatial gas corona comprising 10% of its total mass. The gas is initially in pressure equilibrium with the overall potential and has a spin parameter of $\lambda = 0.16$ (Bullock et al. 2001), with specific angular momentum following $j \propto R$. The dark matter and gas components each consist of 10^6 particles. Each gas particle is initialized with a mass of 1.4×10^5 $M_\odot$ and gravitational softening $\epsilon = 20$ pc, while dark matter particles have a softening length of $\epsilon = 100$ pc and a radially-dependent mass of 10^6 $M_\odot$ within 200 kpc and 3.6×10^6 $M_\odot$ beyond 200 kpc.

After the halos merge, this setup produces a dark matter halo with $r_{200} = 238$ kpc and $M_{200} = 1.6 \times 10^{12}$ $M_\odot$. The hot gas corona has a spin parameter of $\lambda = 0.11$. At this stage, radiative cooling, star formation, and stellar feedback are activated, with the latter represented with the blast-wave prescriptions of Stinson et al. (2006). Gas is converted into stars with 10% efficiency when its density $n > 1$ cm^{-3}, its temperature $T <$ 15 000 K, and it is part of a convergent flow. Each star particle forms with an initial mass of 4.6×10^4 $M_\odot$ and gravitational softening $\epsilon = 20$ pc. Star particles are represented by an entire stellar population with a Miller-Scalo (Miller & Scalo 1979) initial mass function. The evolution of star particles includes asymptotic giant branch (AGB) stellar winds and feedback from Type II and Type Ia supernovae, with their energy injected into the interstellar medium (ISM). Each supernova releases 10^{50} erg into the ISM.

The unwarped simulation corresponds to the M1_c_b model described in Fiteni et al. (2021). It adopts nearly identical initial conditions to one of the progenitor halos in the warped model, but with a lower gas spin parameter ($\lambda = 0.065$), which yields an initially axisymmetric disk. The feedback implementation again follows Stinson et al. (2006), but the supernova energy is set to 4×10^{50} erg and the star formation efficiency is reduced to 5%. The gravitational softening for gas particles is 50 pc.

We evolved both simulations for 12 Gyr, providing complementary warped and unwarped disk systems that allowed direct comparison of the vertical structure and bending wave evolution. Khachaturyants et al. (2022a) demonstrate that both simulations exhibit slow retrograde bending waves, with the amplitudes being larger in the warped model. Fast prograde bending waves are only present in the warped model. In the unwarped model, these prograde modes remain weak, consistent with expectations that they dissipate rapidly via winding. In contrast, the warped simulation maintains substantially stronger prograde waves throughout its evolution, indicating that irregular gas accretion along the warp acted as a sustained driver of vertical perturbations.

In both simulations, a bar and multiple spiral arms form. Khachaturyants et al. (2022a) and Khachaturyants et al. (2022b) provide a detailed analysis of the relative strengths, pattern speeds, and time evolution of the corresponding $m = 2$ density waves.

3. Identifying the phase spirals

After centering the galaxy and aligning the disk with the X–Y plane as described in Khachaturyants et al. (2022a), we selected disk star particles with $Z \in [-2.5, 2.5]$ kpc. To track the evolution of phase space near the Solar radius, we divided an

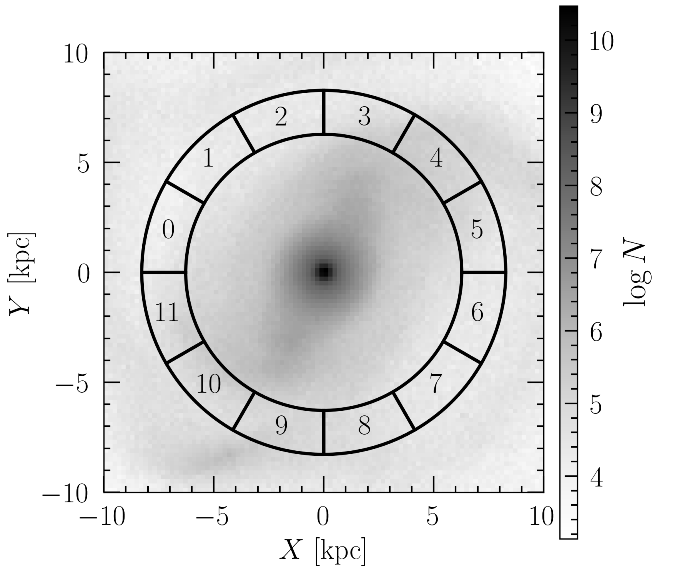

Fig. 1. Twelve regions examined for the presence of phase spirals, projected onto a logarithmic star count map of the simulated warped galaxy at 8.7 Gyr. The regions are equally spaced by 30° in azimuth, at radii between $R = 6.277$ and 8.277 kpc. The regions are labeled from zero to 11 in a clockwise direction. The galaxy rotates counterclockwise.

annulus with galactocentric radius from $R = 6.277$ to 8.277 kpc into 12 regions equally separated by 30° in azimuth, where $R =$ 8.277 kpc is the Solar radius (GRAVITY Collaboration 2022). The galaxy is oriented such that it rotates counterclockwise (positive sense of rotation in a right-handed XYZ coordinate system). Figure 1 shows a stellar number map of the warped simulation at 8.7 Gyr. We show the division of the 12 regions superposed on the map. The regions are labeled from zero to 11 in a clockwise direction.

To identify and characterize phase spirals in the simulation using a standardized method, we adapted the phase spiral finder algorithm from García-Conde et al. (2022). For each region at the Solar radius (Fig. 1), we performed a Fourier decomposition of the stellar distribution in the vertical phase space, Z-V_z. First, we normalized the phase space coordinates Z and V_z by their respective dispersions σ_Z and σ_{V_z}. We denoted the normalized phase space coordinates Z' and V_z'. We calculated the dispersion σ_Z or σ_{V_z} using the robust scatter estimate from Lindegren et al. (2016). We then weighed the normalized histogram by the residual azimuthal velocity, $\Delta V_\phi = V_\phi -$ median(V_ϕ), where we calculated the median(V_ϕ) from the entire phase space histogram[1]. To avoid the influence of outliers on the decomposition, we further selected star particles in a region near the center of the histogram $(Z', V_z') = (0, 0)$ with phase space radius $\tilde{R} \leq 2.6$, where $\tilde{R}(Z', V_z')$ is the Euclidean distance, $\tilde{R} = [(Z')^2 + (V_z')^2]^{1/2}$. We divided the region into $N = 20$ equal-width concentric annuli. We decomposed the weighted density distribution within each annulus into a combination of Fourier modes with $m = 0, \ldots, 6$,

$$\Delta V_\phi(\tilde{R}, \tilde{\phi}) \approx \sum_{m=0}^{6} A_m(\tilde{R}) \sin(m\tilde{\phi} - P_m(\tilde{R})), \qquad (1)$$

[1] We focused on the histogram weighted by median azimuthal velocity, as weighting by median radial velocity (V_R) is prone to being dominated by the quadrupole signatures at the outer phase space radii.

where $\tilde{\phi}(Z', V_z')$ is calculated as $\tilde{\phi} = \arctan2(V_z', Z')$ and P_m is a phase that varies with $\tilde{R}$. Following García-Conde et al. (2022) and Tepper-García et al. (2025), we applied the following constraints to quantitatively identify a significant $m = 1$ phase spiral: A_1/A_0 is higher than any A_m/A_0 for $m \geq 2$; P_1 increases monotonically with $\tilde{R}$; and the scatter around a linear fit for the P_1–$\tilde{R}$ profile is lower than one. We defined the median $m = 1$ Fourier amplitude A_1 as the strength of the phase spiral. If any of the above conditions were not met, we set $A_1 = 0$.

The Fourier decomposition method may result in false positive or false negative detections. In this work, we present conservative results by requiring that the signal-to-noise ratio (S/N) $A_1/\sigma(A_1) \geq 3$, where we bootstrapped the sample of star particles within each annulus 200 times and estimated A_1 and $\sigma(A_1)$ by taking the average and standard deviation of the bootstrapping results. We provide examples of the application of our Fourier decomposition algorithm in Appendix A.4.

In the phase space analysis, we adopted relatively large spatial bins due to the relatively low mass resolution of the simulations in Khachaturyants et al. (2022a) (a few million star particles) compared to pure N-body simulations such as Hunt et al. (2021) and Asano et al. (2025) (more than 200 million disk star particles). Figure 2 provides an example phase spiral with varying mass resolution in the Solar neighborhood ($d_{\rm cyl} \leq$ 0.8 kpc from the Sun) for a high-resolution pure N-body simulation (Asano et al. 2025) at 1.516 Gyr, color-coded by residual azimuthal velocity, ΔV_ϕ. The panels show the full sample (left), randomly selected 15% (middle) and 1% (right) of the sample of 266 978 star particles. Fourier decomposition of the phase space reveals that $A_1 = 1.13 \pm 0.14\,{\rm km\,s^{-1}}$, $1.39 \pm 0.39\,{\rm km\,s^{-1}}$, and $3.47 \pm 1.21\,{\rm km\,s^{-1}}$ for each panel, corresponding to a strong, less prominent, and undetected phase spiral. Figure 2 demonstrates how mass resolution can affect the detectability of phase spirals. We stress that our results describe phase spirals averaged over relatively large regions in the disk of the simulated galaxy.

4. Results

We present the phase spirals detected in the warped and unwarped simulations of Khachaturyants et al. (2022a). We show examples of phase spiral detection in the vertical phase space and study the time evolution of the occurrence of phase spirals in the 12 regions defined in Fig. 1.

4.1. Phase spirals in the warped galaxy

In the *Gaia* DR2 and DR3 data (Gaia Collaboration 2018, 2023b), phase spirals appear in the Z-V_z maps weighted by density contrast, median radial and azimuthal velocities (Antoja et al. 2018; Antoja et al. 2023), and stellar metallicity (Gaia Collaboration 2023a). These phase space maps indicate a strong correlation between the vertical and in-plane velocities of the stars in the local volume, a feature termed "kinematic interlocking" by Tepper-García et al. (2025).

As an example, we present a one-armed phase spiral detected in the warped simulation at 8.7 Gyr. Figure 3 shows the phase spiral in region four (see Fig. 1) of the warped galaxy, weighted by density contrast ($\Delta\rho$), residual azimuthal velocity (ΔV_ϕ), and median radial velocity (V_R). The region contains 36 584 star particles. The normalized phase-space coordinates Z' and V_z' span $[-3, 3]$. We compute the density contrast as $\Delta\rho = H_1/H_2 - 1$, where H_1 and H_2 are the stellar number counts N convolved with Gaussian filters with $\sigma_1 = 1.5$ and $\sigma_2 = 3$, respectively.

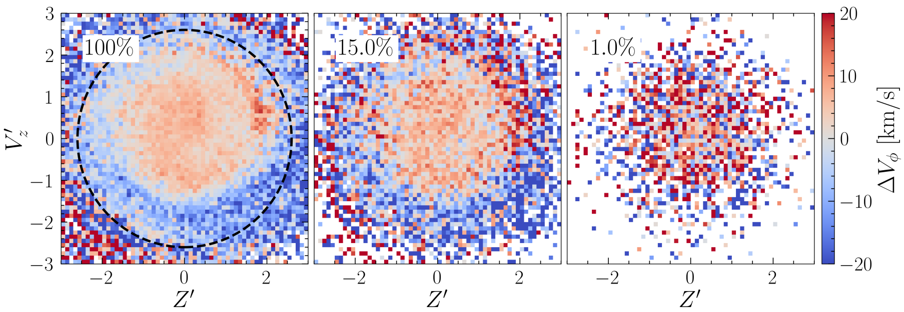

Fig. 2. Example phase spiral observed at varying mass resolution in the Solar neighborhood ($d_{\rm cyl} \leq 0.8$ kpc from the Sun) in a high-resolution pure N-body simulation (Asano et al. 2025) at 1.516 Gyr, color-coded by residual azimuthal velocity, ΔV_ϕ. Panels show the full sample (left), and randomly selected 15% (middle) and 1% (right) subsamples of the full sample of 266 978 star particles. The black circle in the left panel indicates the cutoff at phase space radius $\tilde{R} = 2.6$. The phase spiral is less prominent in the middle panel and undetectable in the right panel.

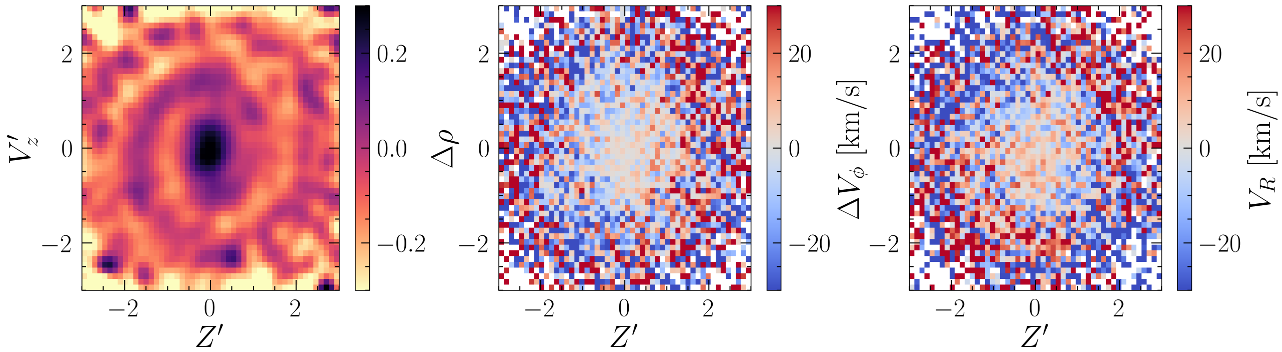

Fig. 3. Phase spiral in region 4 of the warped galaxy at 8.7 Gyr, color-coded by density contrast ($\Delta\rho$), residual azimuthal velocity (ΔV_ϕ), and median radial velocity (V_R), respectively.

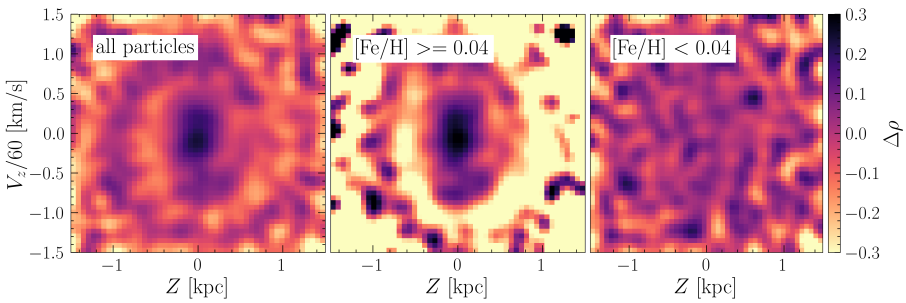

Fig. 4. Phase spiral in region four of the warped galaxy at 8.7 Gyr, color-coded by density contrast (left) and separated into a metal-rich (middle) and a metal-poor (right) subsample at the median metallicity, median([Fe/H]) = 0.04. Axes are scaled as Z/kpc and $V_z/60\,{\rm km\,s^{-1}}$.

The phase spirals weighted by ΔV_ϕ and V_R show kinematic interlocking, consistent with *Gaia* observations.

Figure 4 shows the phase spiral detected in the same region for the entire sample (left), separated into a metal-rich subsample (middle) and a metal-poor subsample (right) at the median metallicity median([Fe/H]) = 0.04. For direct comparison with the observations, we scaled the axes using Z/kpc and $V_z/60\,{\rm km\,s^{-1}}$. We focused on the inner part of the phase space diagram to avoid visual artifacts that could be induced by noise at large phase space radii. Figure 4 shows that the inner part of the phase spiral is more prominent in the metal-rich population than in the metal-poor population, in agreement with observations (Bland-Hawthorn et al. 2019).

Following (Hunt et al. 2022), we binned star particles by the guiding-center radius, R_g, and the azimuthal phase angle, θ_ϕ, to study the spatial variation of the detected phase spirals. We selected star particles with $R \in [3, 13]$ kpc and further constrained the sample to star particles with low radial action, $J_R < {\rm median}(J_R)$, as they exhibit stronger bending waves (Khachaturyants et al. 2022a). We derived the action and angle variables in the analysis as follows. We constructed axisymmetric potential models from a simulation snapshot using `agama`[2] (Vasiliev 2019). We approximated the potential of the dark matter halo and hot gas ($T > 50\,000$ K) using multipole expansions and that of the star particles and cold gas using an azimuthal harmonic expansion. We computed the action and angle variables using the Stäckel Fudge method (Binney 2012) implemented in `agama`.

Figure 5 shows the resulting phase-space maps in the warped galaxy at 8.7 Gyr, color-coded by density contrast. Each normalized phase space coordinate (Z' or V_z') spans the range $[-3, 3]$. The figure provides a clear view of the strong phase spirals across the galaxy. Most of these phase spirals are one-armed, although some exhibit irregular shapes indicative of a superposition of spirals. The morphology of the phase spirals varies with location. Their degree of winding does not vary monotonically with guiding center radius, as expected from an idealized model with a single impact time and no self-gravity

[2] https://github.com/GalacticDynamics-Oxford/Agama

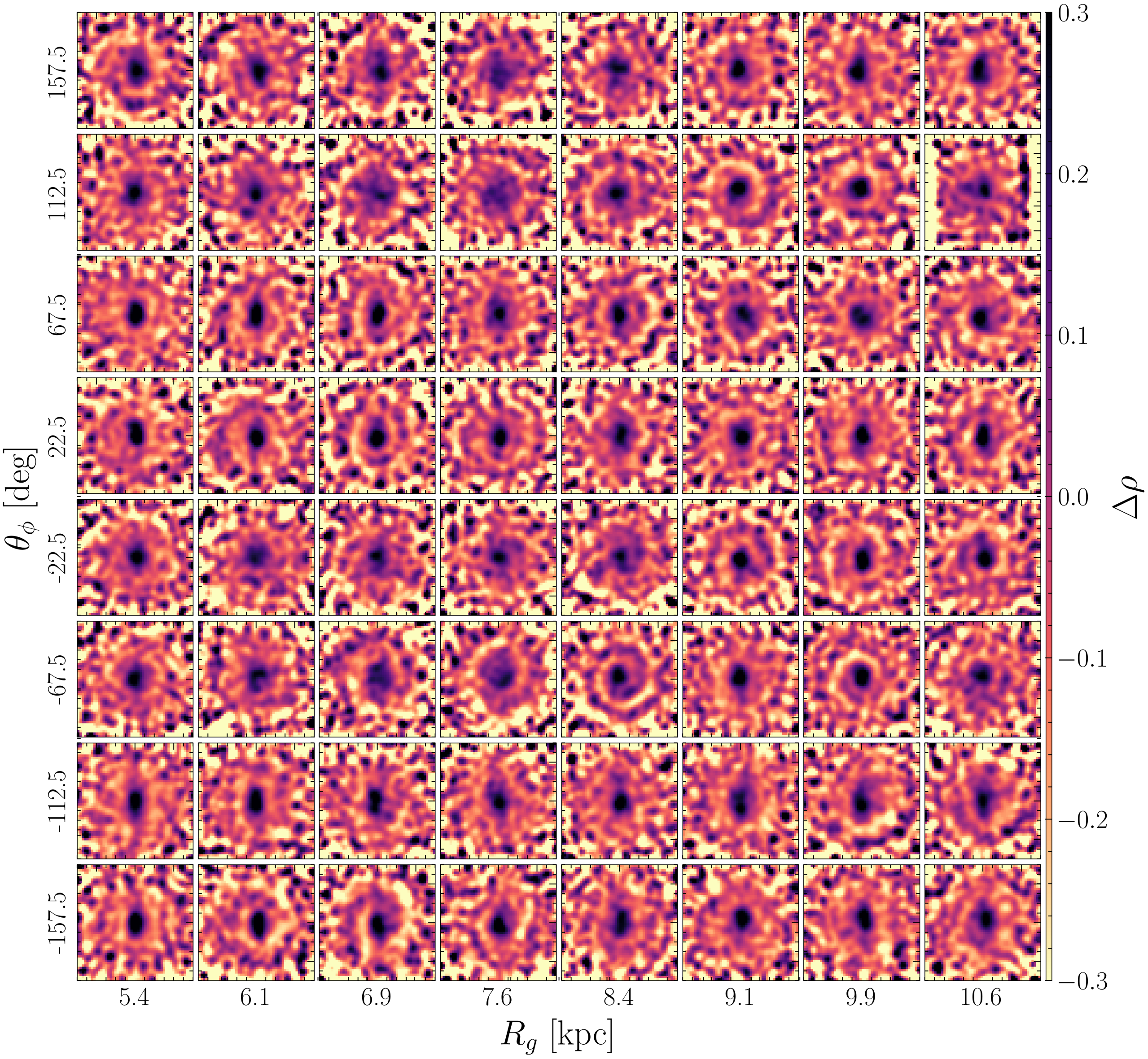

Fig. 5. Phase spirals in the R_g–θ_ϕ plane for star particles with J_R < median(J_R) in the warped galaxy at 8.7 Gyr, color-coded by density contrast. Each normalized phase space coordinate covers the range $[-3, 3]$.

(Widmark et al. 2025). Phase spirals appear to be most tightly wound at $R_g \in [6.9, 9.1]$ kpc. The detected phase spirals do not show a clear "rotation" with respect to the azimuthal phase angle (see Alinder et al. 2023).

Binning star particles in R_g versus θ_ϕ space may introduce biases in the radial action and phase angle, θ_R (e.g., Hunt et al. 2022; Darragh-Ford et al. 2023). The axisymmetric potential approximation may also introduce biases in the radial action (Debattista et al. 2025).

4.2. Phase spiral incidence

Following García-Conde et al. (2022) and Tepper-García et al. (2025), we studied the spatial and time variation of the emergence and strength of the one-armed phase spirals using incidence maps. An incidence map illustrates the occurrence of phase spirals as a function of time and position within the galaxy. The map is an array of cells, where each row corresponds to the 12 regions (Fig. 1) in a particular snapshot, and each column corresponds to different times, allowing us to track the evolution of the phase spirals. Non-empty cells are color-coded by the strength of the phase spiral A_1.

Figure 6 shows the incidence map from 1.91 to 11.61 Gyr for our chosen annulus. At early times (1.91 to 8.51 Gyr), one-armed phase spirals prevail in the warped galaxy. The average phase spiral strength over the 12 regions peaks at approximately 2.8 Gyr, 4.4 Gyr, and 8 Gyr. At late times (8.51–11.61 Gyr), one-armed phase spirals are weaker and less widespread, with only a few isolated detections. In general, the phase spiral incidence varies coherently with azimuth and time, manifesting as upward slopes in the incidence map. The most prominent slope has a period of ~230 Myr. These slopes highlight the azimuthal propagation of the bending waves in the warped simulation.

4.3. Time evolution of phase-spiral incidence rate

We used the incidence rate of the one-armed phase spirals to study their temporal evolution and compared it with that of

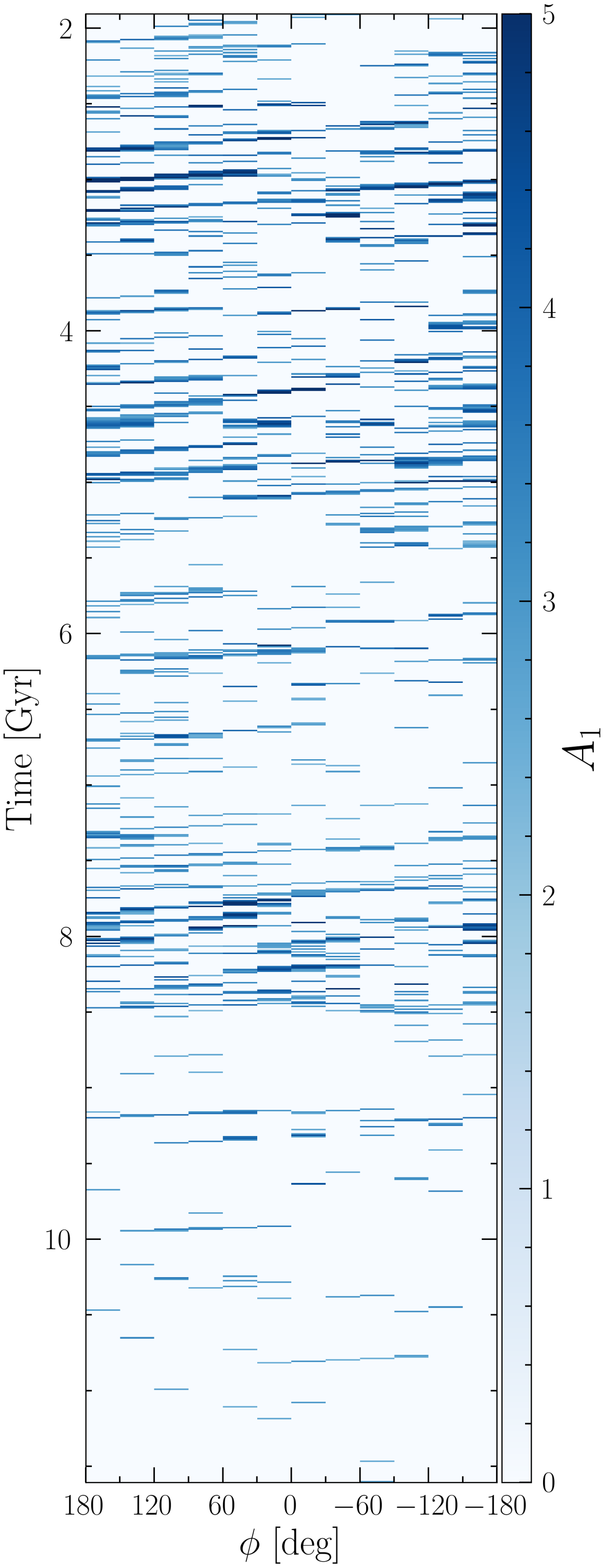

Fig. 6. Incidence map of $m = 1$ phase spirals, weighted by residual V_ϕ, at the 12 regions ($R \in [6.277, 8.277]$ kpc; Fig. 1) in the warped galaxy from 1.91 to 11.61 Gyr. The horizontal axis denotes the azimuth of the region, while the vertical axis denotes the snapshot time. The galaxy rotates from right to left along the horizontal axis.

the gas inflow and bending wave amplitude. We calculated the (dimensionless) phase-spiral incidence rate at a specific time by counting the number of regions with a detected phase spiral and dividing by the total number of regions (12). Figure 7 shows the time evolution of the phase-spiral incidence rate in the warped galaxy versus the gas inflow and bending wave amplitude, from 1.91 to 11.61 Gyr. We calculated the gas inflow as the inward mass flux of cold gas ($T < 50\,000$ K) through a spherical shell with radius $R = 15$ kpc and thickness $\delta R = 0.2$ kpc (Khachaturyants et al. 2022a). We estimated the bending wave amplitude as the root mean square (RMS) of the mean vertical position of the 12 regions, RMS($\langle Z \rangle$). To reduce high frequency noise, we applied a Butterworth filter as implemented in `scipy` with a cutoff period of 0.175 Gyr.

At early times (1.91–8.51 Gyr), the phase-spiral incidence rate evolves with the bending wave amplitude and the gas inflow, displaying a similar triple-peaked behavior. A cross-correlation test between the filtered incidence rate and the gas flux reveals a delay time of approximately 281 Myr. Previous simulations with externally-induced phase spirals (see, e.g., Bland-Hawthorn & Tepper-García 2021; Hunt et al. 2021; Asano et al. 2025) have identified a delay in the formation of phase spirals, consistent with the delay between the bending wave amplitude and the gas flux (approximately 250 Myr at the Solar radius; Khachaturyants et al. 2022a). A similar test shows that the phase-spiral incidence rate evolves with the bending wave amplitude, displaying no significant delay. The high gas inflow at early times induces strong bending waves, resulting in high phase-spiral incidence rates that are on average ~0.15. At late times (8.51–11.61 Gyr), the disk thickens and the gas inflow at the outer disk decreases, resulting in dampened bending waves and low phase-spiral incidence rates.

The warped galaxy forms a bar at ~7.57 Gyr that does not buckle, and one-armed phase spirals are detected well before the formation of the bar. The detected one-armed phase spirals in the warped galaxy are therefore not induced by bar buckling (Khoperskov et al. 2019) in this simulation, but by irregular gas inflow along the warp. In particular, continuous excitation by the warp sustains the phase spirals over the entire evolution of the simulation (~10 Gyr).

4.4. Phase spirals in the unwarped galaxy

This subsection presents the phase spirals detected in the unwarped control simulation. We studied disk star particles with $Z \in [-1, 1]$ kpc. Figure 8 shows the incidence map of the one-armed phase spirals in the unwarped galaxy, weighted by ΔV_ϕ, from 10.75 to 11.71 Gyr. These phase spirals are weak and appear intermittently. Figure 9 illustrates the temporal evolution of the phase-spiral incidence rate in the unwarped galaxy versus that of the bending wave amplitude. The bending waves in the unwarped simulation are significantly weaker than those in the warped simulation (Khachaturyants et al. 2022a). The temporal evolution of the phase-spiral incidence rate does not show a strong correlation with the bending wave amplitude.

Compared to those in the warped galaxy (see Figs. 6 and 7), phase spirals in the unwarped galaxy are weaker, randomly-distributed, and only weakly-correlated with bending waves. Despite the higher mass resolution of the unwarped simulation (~11 million star particles at ~11 Gyr), we did not detect strong phase spirals. The phase spirals in the unwarped simulation may be induced by stochastic heating (Tremaine et al. 2023; Tepper-García et al. 2025) or by weak and spontaneously generated bending waves (Chequers & Widrow 2017; Khachaturyants et al. 2022a).

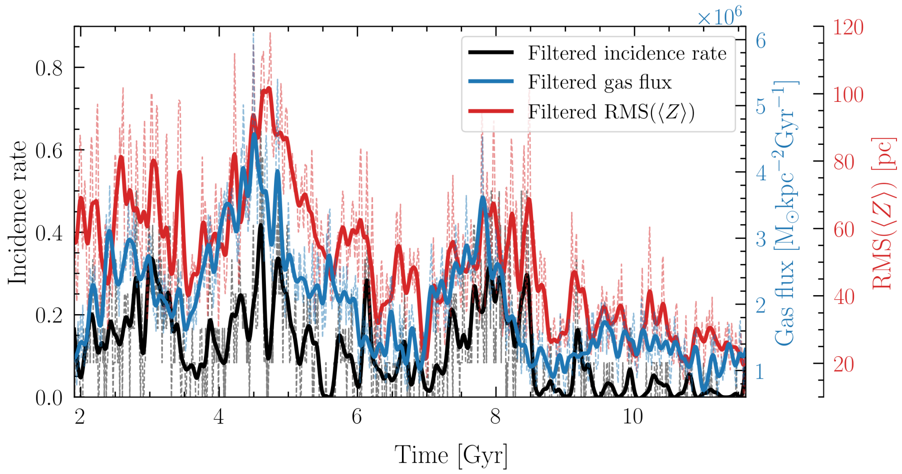

Fig. 7. Time evolution of the phase-spiral incidence rate at $R \in [6.277, 8.277]$ kpc from 1.91 to 11.61 Gyr in the warped galaxy (black dashed line) versus the gas inflow through a spherical shell at 15 kpc (blue dashed line) and the amplitude of bending waves in the same region (red dashed line). We applied a Butterworth filter as implemented in `scipy` with a period of 0.175 Gyr to smooth the signals, where the filtered signals are denoted by thick solid lines.

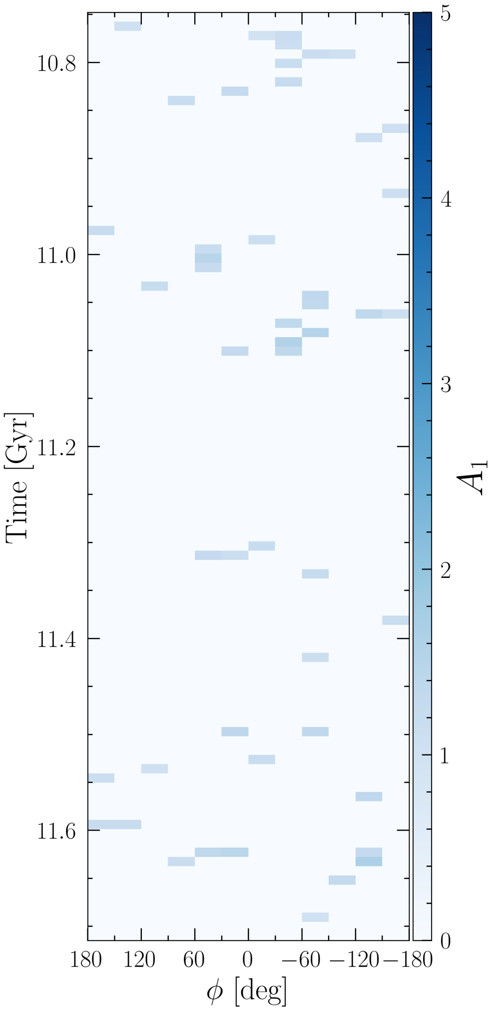

Fig. 8. Incidence map of the $m = 1$ phase spirals, weighted by ΔV_ϕ, at 12 regions in the unwarped galaxy from 10.75 to 11.71 Gyr.

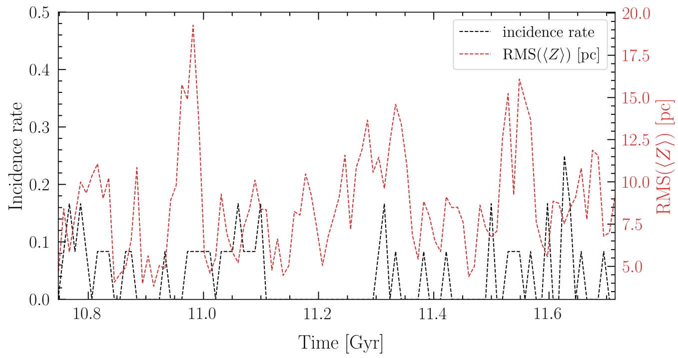

Fig. 9. Time evolution of the phase-spiral incidence rate at $R \in [6.277, 8.277]$ kpc from 10.75 to 11.71 Gyr in the unwarped galaxy (black dashed line) versus the amplitude of the bending waves in the same region (red dashed line).

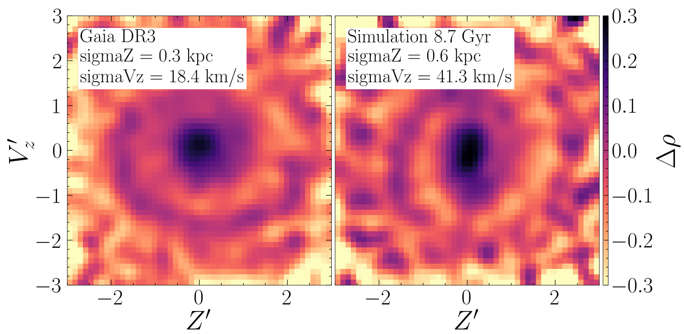

Fig. 10. Phase spiral in the *Gaia* DR3 data compared to that in an equivalent region in the warped galaxy at 8.7 Gyr, color-coded by density contrast. The observational sample contains 55 880 stars. The simulation sample contains 35 989 star particles. Each axis shows the normalized phase space coordinate, covering the range $[-3, 3]$. The vertical position and velocity dispersions of each sample are indicated in the top left corner of each panel.

5. Discussion

5.1. Comparison with Gaia data

To compare the amplitudes of the detected phase spirals in the warped simulation directly with the *Gaia* observations, we randomly selected 100 000 stars within 1 kpc of the Sun from the *Gaia* DR3. We then selected a subsample located within $\phi \in [150, 180]^\circ$, which contains 55 880 stars. We transformed the *Gaia* observables into galactocentric Cartesian coordinates, adopting the same solar position and velocity as in Antoja et al. (2023). Figure 10 compares the phase spiral in the observational sample with a qualitatively similar one within $R \in [7.277, 9.277]$ kpc and $\phi \in [30, 60]^\circ$ of the warped simulation at 8.7 Gyr. The simulation sample contains 35 989 star particles.

The two phase-space maps are color-coded by density contrast using the same color scale. Figure 10 shows that the phase spiral in the simulation sample has an amplitude comparable to that of the observational sample.

An idealized phase-spiral model with a single perturbation time and no self-gravity would produce phase spirals whose winding decreases monotonically with radius (Widmark et al. 2025). The phase spirals observed in the high-resolution simulation of Asano et al. (2025) exhibit similar trends, where those in the inner disk appear to be more tightly-wound than those in the outer disk (see their Figs. 10 and 11). However, the phase spirals observed in the *Gaia* DR3 display a relatively constant radial profile in spiral winding (Widmark et al. 2025). In particular, there are bands of high winding near the local spiral arms. Non-monotonic radial variation of phase-spiral winding also appears in azimuthal action-angle space (e.g., Hunt et al. 2022; Frankel et al. 2023).

In this work, we find that the phase-spiral winding in the warped simulation varies nonmonotonically with guiding center radius (Fig. 5), contrary to the prediction of the idealized model. The discrepancy between our results and the prediction is expected because our phase spirals originate from multiple perturbations in a self-gravitating simulation. The details of the phase-spiral winding in the warped simulation as a function of radius remain to be investigated. Intriguingly, we observe high winding from $R_g = 6.9$ to 9.1 kpc (Fig. 5), although we have not explored the correlation between phase-spiral winding and the location of the spiral arms.

5.2. Impact time analysis

As introduced in Sect. 1, the impact time of a single impulsive perturbation can be inferred from the winding of the resulting phase spirals. Nevertheless, the formation mechanism proposed in this work involves multiple major perturbations. The response of the disk to multiple perturbations can be complex. *N*-body simulations with multiple Sgr passages suggest that the most recent perturbation may “reset” the phase-spiral signature (e.g., Laporte et al. 2019; Bland-Hawthorn et al. 2019), although García-Conde et al. (2022) do not observe a clear reset in their cosmological simulation. Lin et al. (2025) demonstrate that signatures of past perturbations may be preserved in phase space. Most recently, Chiba et al. (2025) propose that the nonlinear coupling of two large-scale perturbations could induce the “Galactic echo” – a second-order response which preserves the phase space imprint of earlier perturbations. If we consider the gas warp as one of the drivers of the observed phase spirals, it further complicates the inference of a single impact time from an impulsive event such as the passage of the Sgr dwarf galaxy.

5.3. Correlation between the phase-spiral incidence rate and other properties

Warp precession rate. Khachaturyants et al. (2022a) measure a slow retrograde precession of the warp in the simulation, at a rate of $\sim -12\ \mathrm{km\,s^{-1}kpc^{-1}}$. Their Fig. 9 shows the time evolution of the $m = 1$ bending signals in the warped simulation, sampled at a time cadence of ∼500 Myr. In this figure, the warp precession rate is nearly constant in time, showing no detectable correlation with the phase-spiral incidence rate in Fig. 7.

Star formation rate. The global star formation history of the warped simulation is provided in Appendix A.1. In Fig. A.1, the global star formation rate shows an overall declining trend with time, showing no clear correlation with the phase-spiral incidence rate in Fig. 7.

5.4. Future prospects

Phase spiral amplitude and winding. Recently, Widmark et al. (2025) developed a method to fully characterize the morphology of phase spirals. In future work, this method could be used to conduct a detailed characterization of the warp-induced phase spirals, which would deepen the understanding of their formation and evolution. Quantitative analysis of the phase-spiral amplitude in the warped simulation enables direct comparison with *Gaia* observations. Analysis of phase-spiral winding provides information on the timing of perturbations across the disk.

Two-armed phase spirals. Two-armed phase spirals are typically associated with breathing modes in the Galaxy (see, e.g., Hunt et al. 2022; Ghosh et al. 2022; Li et al. 2023; Alinder et al. 2024; Asano et al. 2025). Khachaturyants et al. (2022b) identify breathing motions in the warped and unwarped simulations used in this study, although we do not detect clear signatures of two-armed phase spirals. With future higher-resolution simulations, we hope to detect the signatures of two-armed phase spirals.

Macro-spiral. Phase spirals in the warped simulation are widespread as a result of the major perturbation by the warp. Hunt et al. (2021) and Hunt et al. (2024) demonstrate that large-scale perturbations of the disk could generate local phase spirals that collectively form a large-scale phase spiral (the “macro-spiral”). This signature may be key to differentiating between global perturbations and local stochastic kicks.

Perturbation signatures in the gas disk. The limited number of cold gas particles in the gas disk of the warped simulation makes it difficult to analyze their phase space signatures. However, perturbation signatures in the gas disk remain an interesting future prospect.

6. Conclusions

In this work, we present the first discovery of one-armed phase-space spirals in the isolated, warped *N*-body–SPH simulation of Khachaturyants et al. (2022a). We identify these phase spirals in the Z–V_z map weighted by density contrast, residual azimuthal velocity, and median radial velocity. The phase-spiral pattern varies with metallicity, consistent with observations (Bland-Hawthorn et al. 2019). Examining the detected phase spirals in the guiding center radius versus azimuthal phase angle plane shows that they occur globally. The morphology of the phase spirals varies with location. Phase-spiral winding varies nonmonotonically with guiding center radius.

Using a Fourier decomposition algorithm, we quantitatively tracked the time evolution of the one-armed phase spirals in the warped simulation. The incidence map, which illustrates the spatial and time variation of the emergence and strength of the phase spirals, shows that the detected phase spirals are prevalent and long-lived.

We find that the incidence rate of the phase spirals evolves with the gas inflow at the outer disk and the bending wave amplitude. In particular, the phase-spiral incidence rate lags the gas inflow by a few hundred Myr, consistent with estimates from the literature for the delay between the perturbation and the emergence of phase spirals (see, e.g., Bland-Hawthorn & Tepper-García 2021; Hunt et al. 2021; Tepper-García et al. 2025; Asano et al. 2025). There is no significant delay between the incidence rate and the bending wave amplitude. Hence, we propose that the detected one-armed phase spirals are signatures of the bending waves induced by irregular gas accretion along the warp. Repeated excitations by the warp sustain the phase spirals for ~10 Gyr, which implies that in this scenario there is no single perturbation time.

We also detect phase spirals in the unwarped simulation. These phase spirals are weak and stochastically-distributed, and their incidence rate shows no strong correlation with the bending wave amplitude. They are likely induced by stochastic heating or weak bending waves.

We show that warp-induced phase spirals have amplitudes consistent with those in the *Gaia* observations, although a more quantitative analysis is required.

Higher-resolution *N*-body–SPH simulations and quantitative analysis of the characteristics of the warp-induced phase spiral will allow us to characterize the phase spirals in more detail and provide further insight into the interpretation of *Gaia* observations.

Acknowledgements. We thank the referee for the insightful suggestions that improved this manuscript. SW greatly appreciates the helpful discussions at the Lorentz Center workshop 'Winding, Unwinding and Rewinding the *Gaia* Phase Spiral'. SW is grateful to E. Vasiliev for his insightful suggestions on the potential approximation and to T. Asano for providing access to the simulation data from Asano et al. (2025). This project has received funding from the European Union's Horizon 2020 research and innovation programme under the Marie Skłodowska-Curie grant agreement No. 101072454 (MWGaiaDN). The simulations in this paper were run at the DiRAC Shared Memory Processing System at the University of Cambridge, operated by the COSMOS Project at the Department of Applied Mathematics and Theoretical Physics on behalf of the STFC DiRAC HPC Facility (`www.dirac.ac.uk`). This equipment was funded by BIS National E-infrastructure capital grant ST/J005673/1, STFC capital grant ST/H008586/1, and STFC DiRAC Operations grant ST/K00333X/1. DiRAC is part of the National E-Infrastructure. Preliminary analysis was carried out on Stardynamics, a 64- core machine that was funded from Newton Advanced Fellowship NA150272 awarded by the Royal Society and the Newton Fund. This work has made use of data from the European Space Agency (ESA) mission *Gaia* (`https://www.cosmos.esa.int/gaia`), processed by the *Gaia* Data Processing and Analysis Consortium (DPAC, `https://www.cosmos.esa.int/web/gaia/dpac/consortium`). Funding for the DPAC has been provided by national institutions, in particular the institutions participating in the *Gaia* Multilateral Agreement. This work made use of the following software: `astropy` (Astropy Collaboration 2013, 2018), `matplotlib` (Hunter 2007), `scipy` (Virtanen et al. 2020), and `numpy` (Harris et al. 2020). The processing of the simulations was performed with the Python library `pynbody` (Pontzen et al. 2013).

References

Alinder, S., McMillan, P. J., & Bensby, T. 2023, A&A, 678, A46
Alinder, S., McMillan, P. J., & Bensby, T. 2024, A&A, 690, A15
Antoja, T., Helmi, A., Romero-Gómez, M., et al. 2018, Nature, 561, 360
Antoja, T., Ramos, P., García-Conde, B., et al. 2023, A&A, 673, A115
Asano, T., Fujii, M. S., Baba, J., Portegies Zwart, S., & Bédorf, J. 2025, A&A, 700, A109
Astropy Collaboration (Robitaille, T. P., et al.) 2013, A&A, 558, A33
Astropy Collaboration (Price-Whelan, A. M., et al.) 2018, AJ, 156, 123
Banik, U., van den Bosch, F. C., & Weinberg, M. D. 2023, ApJ, 952, 65
Binney, J. 2012, MNRAS, 426, 1324
Binney, J., & Schönrich, R. 2018, MNRAS, 481, 1501
Bland-Hawthorn, J., & Tepper-García, T. 2021, MNRAS, 504, 3168
Bland-Hawthorn, J., Sharma, S., Tepper-Garcia, T., et al. 2019, MNRAS, 486, 1167
Bullock, J. S., Dekel, A., Kolatt, T. S., et al. 2001, ApJ, 555, 240
Chequers, M. H., & Widrow, L. M. 2017, MNRAS, 472, 2751
Chiba, R., Ding, J., Hamilton, C., Kunz, M. W., & Tremaine, S. 2025, MNRAS, 543, 190
Chiba, R., Frankel, N., & Hamilton, C. 2025, MNRAS, 543, 2159
Darling, K., & Widrow, L. M. 2018, MNRAS, 484, 1050
Darragh-Ford, E., Hunt, J. A. S., Price-Whelan, A. M., & Johnston, K. V. 2023, ApJ, 955, 74
Debattista, V. P., van den Bosch, F. C., Roškar, R., et al. 2015, MNRAS, 452, 4094
Debattista, V. P., Khachaturyants, T., Amarante, J. A. S., et al. 2025, MNRAS, 537, 1620
Fiteni, K., Caruana, J., Amarante, J. A. S., Debattista, V. P., & Beraldo e Silva, L. 2021, MNRAS, 503, 1418
Frankel, N., Bovy, J., Tremaine, S., & Hogg, D. W. 2023, MNRAS, 521, 5917
Gaia Collaboration (Brown, A. G. A., et al.) 2018, A&A, 616, A1
Gaia Collaboration (Recio-Blanco, A., et al.) 2023a, A&A, 674, A38
Gaia Collaboration (Vallenari, A., et al.) 2023b, A&A, 674, A1
García-Conde, B., Roca-Fàbrega, S., Antoja, T., Ramos, P., & Valenzuela, O. 2022, MNRAS, 514, 1801
García-Conde, B., Antoja, T., Roca-Fàbrega, S., et al. 2024, A&A, 683, A47
Ghosh, S., Debattista, V. P., & Khachaturyants, T. 2022, MNRAS, 511, 784
Gilman, D., Bovy, J., Frankel, N., & Benson, A. 2025, ApJ, 980, 24
Grand, R. J. J., Pakmor, R., Fragkoudi, F., et al. 2023, MNRAS, 524, 801
GRAVITY Collaboration (Abuter, R., et al.) 2022, A&A, 657, L12
Guo, R., Li, Z.-Y., Shen, J., Mao, S., & Liu, C. 2024, ApJ, 960, 133
Harris, C. R., Millman, K. J., van der Walt, S. J., et al. 2020, Nature, 585, 357
Hunt, J. A. S., Price-Whelan, A. M., Johnston, K. V., & Darragh-Ford, E. 2022, MNRAS, 516, L7
Hunt, J. A. S., Stelea, I. A., Johnston, K. V., et al. 2021, MNRAS, 508, 1459
Hunt, J. A. S., Price-Whelan, A. M., Johnston, K. V., et al. 2024, MNRAS, 527, 11393
Hunt, J. A. S., & Vasiliev, E. 2025, New A Rev., 100, 101721
Hunter, J. D. 2007, Comput. Sci. Eng., 9, 90
Khachaturyants, T., Beraldo e Silva, L., Debattista, V. P., & Daniel, K. J. 2022a, MNRAS, 512, 3500
Khachaturyants, T., Debattista, V. P., Ghosh, S., Beraldo e Silva, L., & Daniel, K. J. 2022b, MNRAS, 517, L55
Khoperskov, S., Di Matteo, P., Gerhard, O., et al. 2019, A&A, 622, L6
Laporte, C. F. P., Minchev, I., Johnston, K. V., & Gómez, F. A. 2019, MNRAS, 485, 3134
Li, C., Siebert, A., Monari, G., Famaey, B., & Rozier, S. 2023, MNRAS, 524, 6331
Lin, J., Li, Z.-Y., Guo, R., et al. 2025, ApJ, 988, 254
Lindegren, L., Lammers, U., Bastian, U., et al. 2016, A&A, 595, A4
Miller, G. E., & Scalo, J. M. 1979, ApJS, 41, 513
Navarro, J. F., Frenk, C. S., & White, S. D. M. 1996, ApJ, 462, 563
Pontzen, A., Roškar, R., Stinson, G. S., et al. 2013, pynbody: Astrophysics Simulation Analysis for Python, astrophysics Source Code Library [`record ascl:1305.002`]
Stinson, G., Seth, A., Katz, N., et al. 2006, MNRAS, 373, 1074
Tepper-García, T., Bland-Hawthorn, J., Bedding, T. R., Federrath, C., & Agertz, O. 2025, MNRAS, 542, 1987
Tremaine, S., Frankel, N., & Bovy, J. 2023, MNRAS, 521, 114
Vasiliev, E. 2019, MNRAS, 482, 1525
Vasiliev, E., & Belokurov, V. 2020, MNRAS, 497, 4162
Virtanen, P., Gommers, R., Oliphant, T. E., et al. 2020, Nat. Methods, 17, 261
Wadsley, J. W., Stadel, J., & Quinn, T. 2004, New A, 9, 137
Widmark, A., Laporte, C., & de Salas, P. F. 2021, A&A, 650, A124
Widmark, A., Tavangar, K., Kalish, J., Johnston, K. V., & Hunt, J. A. S. 2025, arXiv e-prints [arXiv:`2507.19579`]
Widrow, L. M. 2023, MNRAS, 522, 477

Appendix A: Supplementary figures

A.1. Star formation history

Figure A.1 shows the global star formation history (SFH) of the warped simulation. The global star formation rate (SFR) shows an overall declining trend with time. The SFR in Fig. A.1 appears slightly higher than that in the Milky Way, because the warped simulation in Khachaturyants et al. (2022a) was run with a low density threshold for star formation in order to increase the number of star particles forming within the warp.

A.2. Velocity profiles

The left panel of Fig. A.2 shows the mass-averaged azimuthal velocity profile of the star particles and cold gas ($T < 50\,000$ K), as well as the circular velocity ($V_{\rm circ}$) profile for all particles (star particles, gas and dark matter) in the warped simulation at 8.7 Gyr and that calculated from the approximated potential using `agama`. The right panel shows the radial (σ_R), azimuthal (σ_ϕ) and vertical velocity dispersion (σ_Z) profiles of the same simulation snapshot.

A.3. Phase spirals in the R_g-θ_ϕ plane (high J_R population)

Figure A.3 shows the detected phase spirals in the R_g-θ_ϕ plane for star particles with high radial action. These star particles are dynamically old, exhibit weaker bending waves (Khachaturyants et al. 2022a) and less prominent phase spiral signatures.

A.4. Examples of the Fourier decomposition algorithm

We use analytical one-armed phase spirals to validate the phase spiral finder algorithm. We create a 100×100 grid in the vertical phase space with $Z \in [-3, 3]$ kpc and $V_z \in [-120, 120]\,{\rm km\,s^{-1}}$. We add Gaussian noise to simulate the vertical position and velocity dispersions, with $\sigma_Z = 1$ kpc and $\sigma_{V_z} = 60\,{\rm km\,s^{-1}}$, respectively. The analytical expression simulating a one-armed phase spiral in the mock ΔV_ϕ-weighted phase space is:

$$\Delta V_\phi(\tilde{R}, \tilde{\phi}) = A_1(\tilde{R}) \sin(\tilde{\phi} - P_1(\tilde{R})), \tag{A.1}$$

where A_1 and P_1 linearly increase with $\tilde{R}$. After generating the analytical phase spiral, we apply the phase spiral finder algorithm and Fourier decompose the normalized phase space diagram.

Figure A.4 shows the result of Fourier decomposing the analytical one-armed phase spiral with $A_1(\tilde{R}) = -10\tilde{R}$ and $P_1(\tilde{R}) = 0.5\pi\tilde{R}$. The plot demonstrates the effectiveness of the algorithm in the identification of one-armed phase spirals.

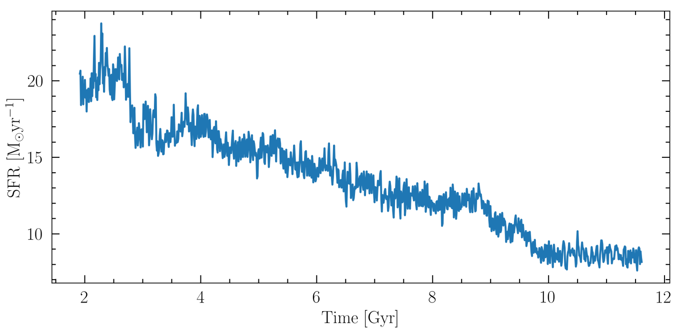

Fig. A.1: Global star formation history of the warped simulation.

Figure A.5 shows the result of Fourier decomposing the ΔV_ϕ-weighted phase space map in Fig. 3 (region 4 in the warped galaxy at 8.7 Gyr). The dominant A_1 and linearly increasing ϕ_1 correspond to a positive detection of a one-armed phase spiral.

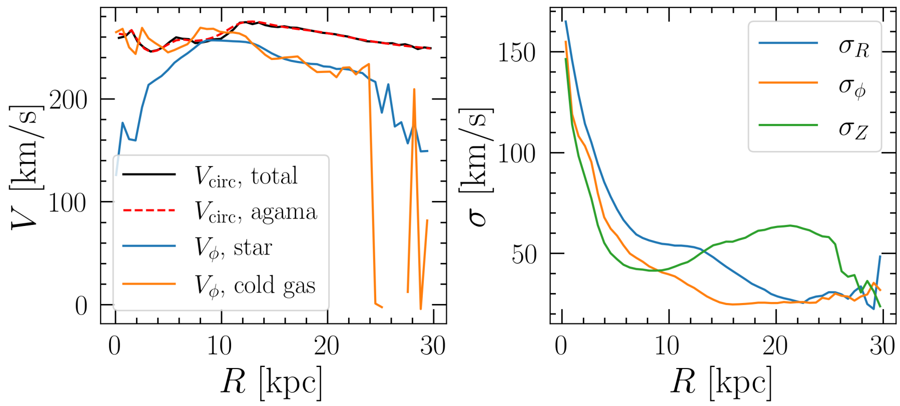

Fig. A.2: Left: the mass-averaged azimuthal velocity profile of the star particles (blue solid line) and cold gas (orange solid line), as well as the circular velocity ($V_{\rm circ}$) profile for all particles in the warped simulation at 8.7 Gyr (black solid line) and that calculated from the approximated potential using `agama` (red dashed line); Right: The mass-averaged radial (σ_R), azimuthal (σ_ϕ) and vertical velocity dispersion (σ_Z) profiles of the same simulation snapshot.

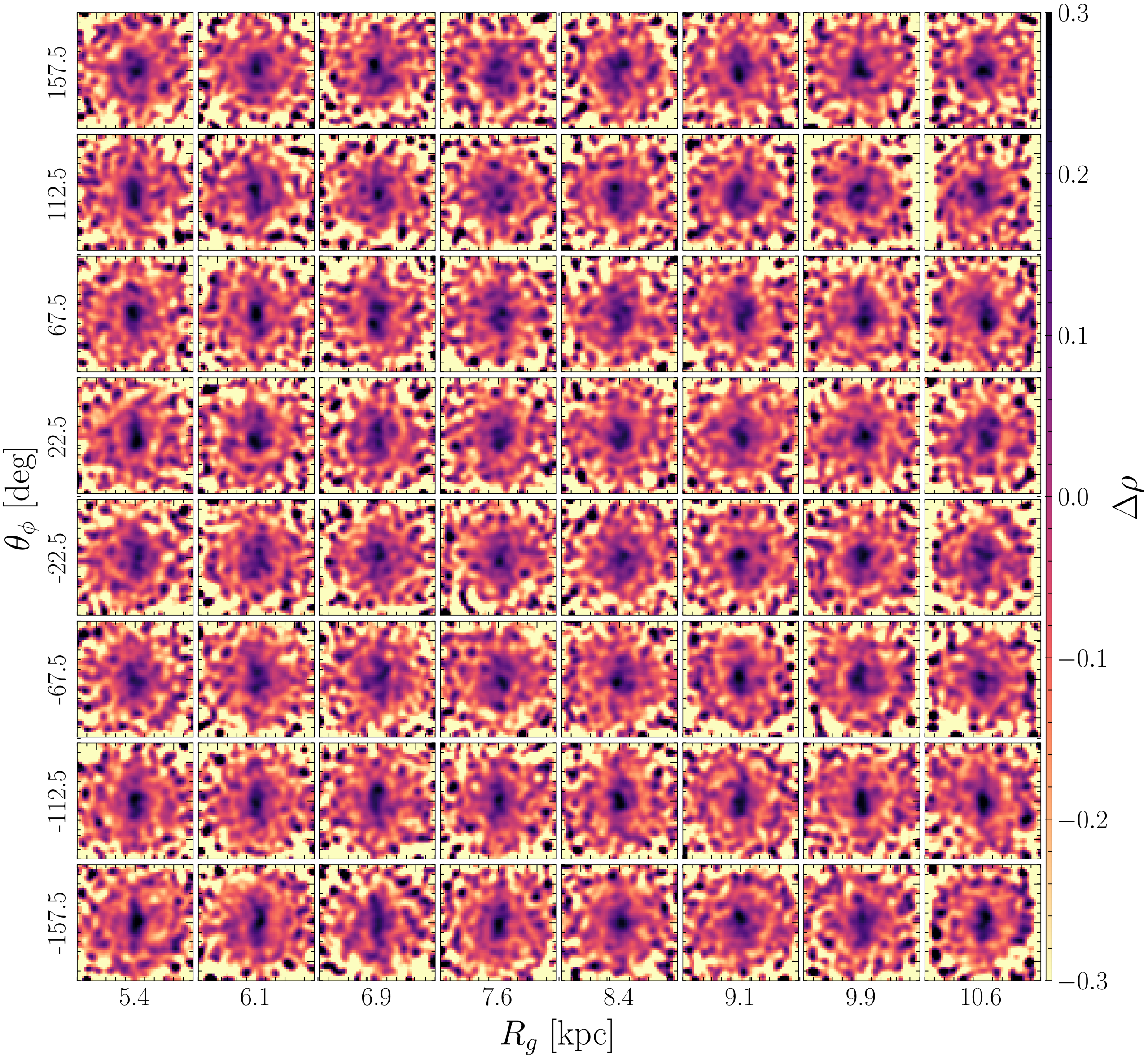

Fig. A.3: The phase spirals in the R_g-θ_ϕ plane for star particles with J_R > median(J_R) at 8.7 Gyr in the warped galaxy, color-coded by density contrast.

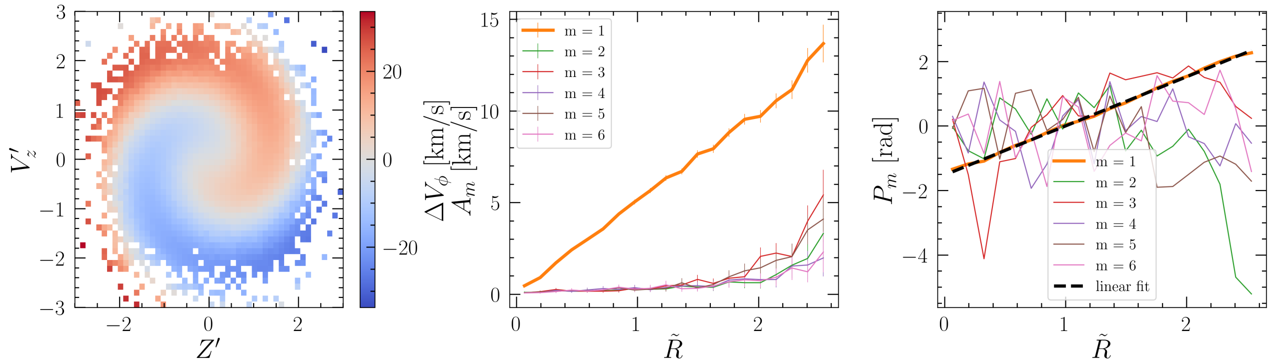

Fig. A.4: Left: mock ΔV_ϕ-weighted phase space map for an idealized one-armed phase spiral. Middle and right: the result of Fourier decomposing the phase space map. Middle: Fourier amplitude versus phase space radius with $m = 1, \cdots, 6$. Error bars are calculated by bootstrapping the sample of star particles within each annulus 200 times. Right: Fourier phase angle versus phase space radius. The black dashed line shows a linear fit to the $m = 1$ P_1-$\tilde{R}$ curve.

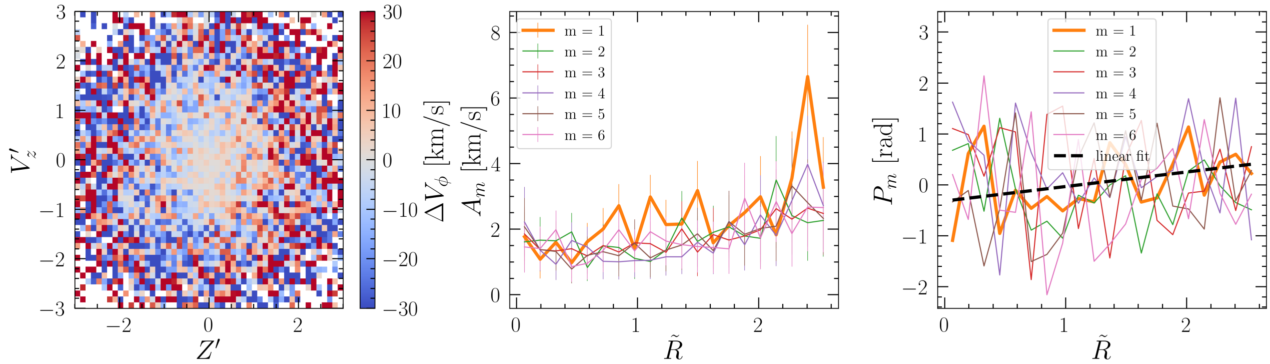

Fig. A.5: Left: ΔV_ϕ-weighted phase space diagram in region 4 of the warped galaxy at 8.7 Gyr. Middle: the radial profile of the Fourier amplitude, for $m = 1, \cdots, 6$. Right: the radial profile of the Fourier phase angle. The black dashed line shows a linear fit to the $m = 1$ P_1-$\tilde{R}$ curve.